

# $K^-N$ amplitudes below threshold constrained by multinucleon absorption

E. Friedman<sup>a,\*</sup>, A. Gal<sup>a</sup>

<sup>a</sup>*Racah Institute of Physics, The Hebrew University, 91904 Jerusalem, Israel*

---

## Abstract

Six widely different subthreshold  $K^-N$  scattering amplitudes obtained in SU(3) chiral-model EFT approaches by fitting to low-energy and threshold data are employed in optical-potential studies of kaonic atoms. Phenomenological terms representing  $K^-$  multinucleon interactions are added to the EFT-inspired single-nucleon part of the  $K^-$ -nucleus optical potential in order to obtain good fits to kaonic-atom strong-interaction level shifts and widths across the periodic table. Introducing as a further constraint the fractions of single-nucleon  $K^-$  absorption at rest from old bubble-chamber experiments, it is found that only two of the models considered here reproduce these absorption fractions. Within these two models, the interplay between single-nucleon and multinucleon  $K^-$  interactions explains features observed previously with fully phenomenological optical potentials. Radial sensitivities of kaonic atom observables are re-examined, and remarks are made on the role of ‘subthreshold kinematics’ in absorption-at-rest calculations.

*Keywords:*  $K^-$ -nucleon and  $K^-$ -nucleus interaction; Near threshold energies; Kaonic atoms; Absorption at rest

---

## 1. Introduction

Several SU(3) chiral-model EFT approaches to the  $\bar{K}$ -nucleon interaction have been presented in recent years, demonstrating good agreement with each other at threshold and above, where they are constrained by some  $K^-p$  low-energy scattering and reaction data. At threshold, the precise measurement of strong-interaction level shift and width of the  $1s$  state in the kaonic atom

---

\*Corresponding author: E. Friedman, elifried@cc.huji.ac.il

of hydrogen by the SIDDHARTA collaboration [1, 2] provides an important constraint on the  $K^-p$  interaction, in addition to three previously known threshold branching ratios. However, as shown recently [3, 4] the resulting  $K^-N$  scattering amplitudes appear to be strongly model dependent when extrapolating to energies below threshold and also with respect to their pole content. Moreover, for the  $K^-n$  amplitude different models predict widely different results both below threshold and above.

An algorithm for constructing self-consistently the density dependent single-nucleon part  $V_{K^-}^{(1)}(\rho)$  of the  $K^-$ -nucleus optical potential  $V_{K^-}(\rho)$  from energy dependent  $\bar{K}N$  amplitudes was presented by Cieplý et al. [5, 6]. For the predominantly attractive  $\bar{K}N$  interaction, the  $\bar{K}N$  energies involved in kaonic atoms are below threshold, leading to a well defined in-medium ‘sub-threshold kinematics’ scheme, as practised in our recent analyses of kaonic atom data [7, 8]. For lack of accepted microscopic theory, this approach cannot be applied to the multinucleon part  $V_{K^-}^{(2)}(\rho)$  of  $V_{K^-}(\rho)$ , which usually consists of phenomenological terms devised to achieve agreement with experiment, as reviewed in Refs. [9, 10].

In the present work we consider six different  $K^-N$  amplitudes derived in several EFT SU(3) chiral-model approaches to  $\mathcal{S}=-1$  meson-baryon interactions and studied recently for their pole content [3]. Augmented by phenomenological amplitudes that could be identified with multinucleon processes, these six single-nucleon model amplitudes are used to describe strong interaction observables in kaonic atoms. These observables include for the first time some old experimental results from bubble chambers on absorption at rest of  $K^-$  mesons on nuclei [11, 12, 13]. Specifically, we calculate the *fraction* of absorptions on a single nucleon out of all absorptions at rest in kaonic atoms, and compare with these experimental results in order to place a new constraint on the  $K^-N$  model-amplitudes input. While this topic was discussed for  $^{12}\text{C}$  [14] and in nuclear matter [15], the present study is the first realistic kaonic atoms calculation that considers single-nucleon absorption fractions across the periodic table.

The paper is organized as follows. Section 2 introduces the  $K^-N$  model-amplitudes input and the in-medium ‘subthreshold kinematics’ methodology as applied to kaonic atoms, followed by the topic of single-nucleon fractions of absorption at rest. Section 3 provides results, showing that only two of the six sets of  $K^-N$  amplitudes are acceptable when fractions of single-nucleon vs. multinucleon absorption are considered in kaonic atoms studies. The two

acceptable sets of amplitudes turn out to be quite similar, and in section 4 we discuss in detail the interplay between the single-nucleon amplitudes and the full optical potential based on these two sets of amplitudes. Radial sensitivities of kaonic atom observables are re-examined, and remarks are made on the role that ‘subthreshold kinematics’ plays in absorption-at-rest calculations. A brief summary is presented in section 5.

## 2. Input and methodology

### 2.1. Input $K^-N$ amplitudes

The  $K^-N$  amplitudes considered in the present work have been derived in various strangeness  $\mathcal{S}=-1$  chiral SU(3) meson-baryon coupled-channel dynamical model approaches at next-to-leading order (NLO). Our specific choice follows that by Cieplý et al. [3] in their recent pole-content study of six such amplitudes generated in four different models, [16, 17, 18, 19] in chronological order. At NLO, the meson-baryon interaction consists of contact terms, parametrized by low-energy constants (LEC) which are fitted to low-energy  $K^-p$  scattering and reaction cross sections, to three precisely determined threshold branching ratios, and also to the kaonic hydrogen energy shift and width as measured recently at the DAΦNE  $e^+e^-$  collider in Frascati by the SIDDHARTA Collaboration [1, 2]. These NLO fitted LEC are added to the leading-order (LO) Weinberg-Tomozawa (WT) term plus the Born graphs contributions. For a recent review, see Ref. [4]. The six  $K^-N$   $s$ -wave center-of-mass (c.m.) amplitudes considered in the present work are plotted in Figs. 1 (real parts) and 2 (imaginary parts) as a function of the c.m. energy  $\sqrt{s}$  below and above threshold for both  $K^-p$  (upper panels) and  $K^-n$  (lower panels).

For  $K^-p$ , all the models agree at threshold, and three out of the four models also agree above threshold where they were essentially fitted to data. The Bonn model amplitudes, however, differ from the other ones above threshold, apparently because higher partial waves were allowed in the fitting procedure. All the amplitudes differ appreciably when going to subthreshold energies. For  $K^-n$ , there are substantial differences between any two of the plotted amplitudes over the full energy range shown. For M2, in particular, the imaginary amplitude is not even positive definite. Thus, below threshold where one derives the input  $K^-N$  amplitudes for kaonic-atom calculations (see next subsection) all six amplitudes shown in Figs. 1 and 2 are different, providing thereby an interesting model dependence to explore.

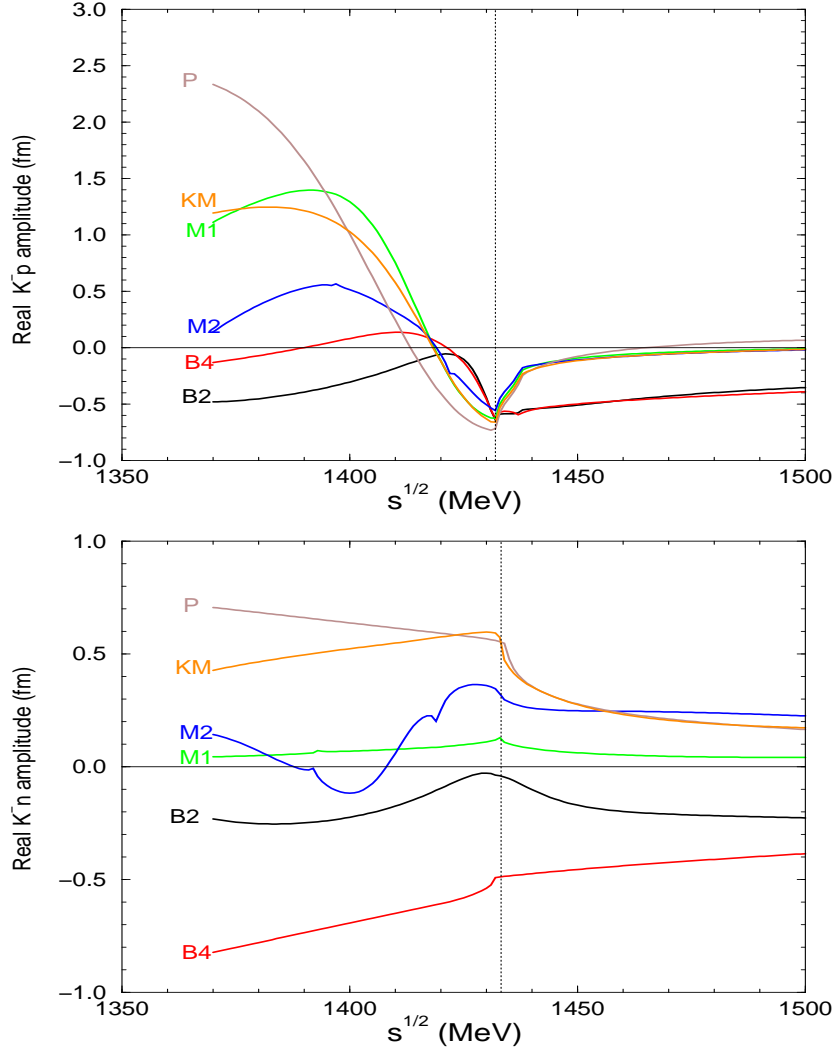


Figure 1: Color online. Real part of six  $K^-N$   $s$ -wave amplitudes used in the present work, taken from chiral SU(3) meson-baryon coupled-channel dynamical models discussed in [3] and denoted there by KM for Kyoto-Munich [16], P for Prague [17], M1 and M2 for Murcia [18], and B1 and B2 for Bonn [19]. Vertical dotted lines indicate threshold energies.

The Kyoto-Munich (KM) and Prague (P)  $K^-N$  amplitudes were used already in our previous kaonic atom studies [7, 8], yielding similar results to each other, but within a different context than the present one. These two amplitudes also happen to satisfy the absorption-at-rest constraint imposed

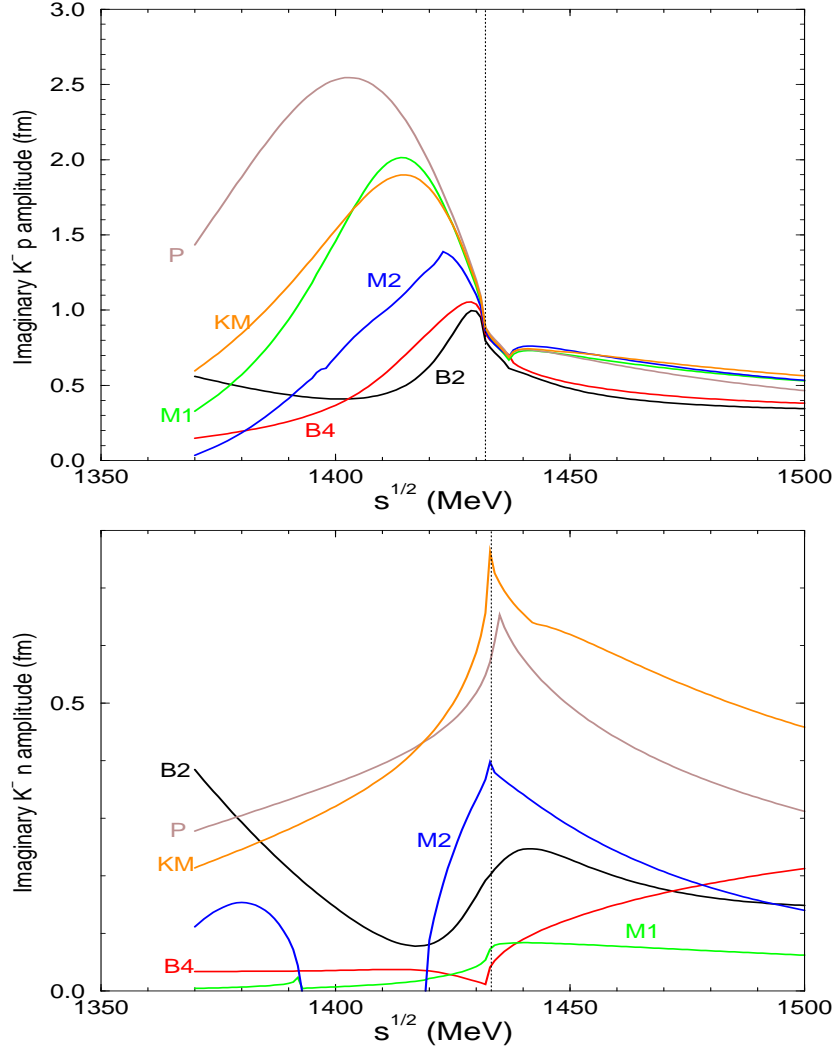


Figure 2: Color online. Imaginary part of six  $K^- N$   $s$ -wave amplitudes used in the present work. Notations follow those in Fig. 1. Vertical dotted lines indicate threshold energies.

in the present work. Interestingly, the KM and P NLO amplitudes are only moderately different from their LO WT variants, in contrast to the Murcia (M) and Bonn (B) amplitudes with sizable NLO contributions. As noted in Ref. [3], the available low-energy  $K^- p$  data do not exclude large NLO contributions, although good reproduction of these data was reached already

at the LO level. In this respect, the Prague and Kyoto-Munich models are the more conservative among the models surveyed here.

## 2.2. Subthreshold kinematics

The model underlying the subthreshold energy algorithm adopts the Mandelstam variable  $s = (E_{K^-} + E_N)^2 - (\vec{p}_{K^-} + \vec{p}_N)^2$  as the argument transforming free-space to in-medium  $K^-N$  amplitudes, where both the  $K^-$  and the nucleon variables are determined independently by the respective environment of a  $K^-$  atom and a nucleus. Consequently, unlike in the two-body c.m. system, here  $\vec{p}_{K^-} + \vec{p}_N$  does not vanish, and one gets to a good approximation  $(\vec{p}_{K^-} + \vec{p}_N)^2 \rightarrow p_{K^-}^2 + p_N^2$  upon averaging over angles. Energies are given by

$$E_{K^-} = m_{K^-} - B_{K^-}, \quad E_N = m_N - B_N, \quad (1)$$

where  $m$  denotes masses and  $B$  denotes binding energies. For the  $K^-$  momentum we substitute locally

$$\frac{p_{K^-}^2}{2m_{K^-}} = -B_{K^-} - \text{Re } V_{K^-} - V_c, \quad (2)$$

where  $V_{K^-}$  is the  $K^-$ -nucleus optical potential and  $V_c$  is the  $K^-$  Coulomb potential due to the finite-size nuclear charge distribution. For the nucleon momentum  $p_N$  we adopt the Fermi gas model (FGM), yielding in the local density approximation

$$\frac{p_N^2}{2m_N} = T_N (\rho/\bar{\rho})^{2/3}, \quad (3)$$

where  $\rho$  is the local density,  $\bar{\rho}$  is the average nuclear density and  $T_N$  is the average nucleon kinetic energy which assumes the value 23 MeV in the FGM.

Defining  $\delta\sqrt{s} = \sqrt{s} - E_{\text{th}}$  with  $E_{\text{th}} = m_{K^-} + m_N$ , and applying the minimal substitution requirement [20, 21]  $E \rightarrow E - V_c$ , then to first order in  $B/E_{\text{th}}$  and  $(p/E_{\text{th}})^2$  one gets

$$\delta\sqrt{s} = -B_N\rho/\bar{\rho} - \beta_N[T_N(\rho/\bar{\rho})^{2/3} + B_{K^-}\rho/\rho_0 + V_c(\rho/\rho_0)^{1/3}] + \beta_{K^-}\text{Re } V_{K^-}, \quad (4)$$

with  $\beta_N = m_N/(m_N + m_{K^-})$ ,  $\beta_{K^-} = m_{K^-}/(m_N + m_{K^-})$ , and  $\rho_0 = 0.17 \text{ fm}^{-3}$ . Following previous applications [5, 6, 7, 8] an average binding energy value of  $B_N = 8.5 \text{ MeV}$  is used. The specific  $\rho/\rho_0$  and  $\rho/\bar{\rho}$  forms of density dependence ensure that  $\delta\sqrt{s} \rightarrow 0$  when  $\rho \rightarrow 0$  [8] in accordance with the low-density limit.

### 2.3. In-medium amplitudes

Eq. (4) defines energy as function of a local density where the optical potential is part of the argument. In the ‘ $t\rho$ ’ approximation (see below) the potential depends on the  $K^-N$  amplitudes that in turn depend on the potential through the energy  $\sqrt{s}$ . Therefore an iterative solution of Eq. (4) is required. Experience shows that convergence is achieved after 4-6 iterations, yielding the energy  $\sqrt{s}$  as function of density  $\rho$  to serve as the argument for calculating the amplitudes.

Final steps towards a calculation of a ‘ $t\rho$ ’ optical potential are the transformation from the  $K^-N$  system to the  $K^-$ -nucleus system and incorporating Pauli correlations, which are the longest-range correlations in the nuclear medium, from Ref. [22]. The ‘ $t\rho$ ’ in-medium single-nucleon optical potential  $V_{K^-}^{(1)}(\rho)$ , including Pauli correlations, is given by [8]

$$2\mu_K V_{K^-}^{(1)}(\rho) = -4\pi \left[ \frac{(2\tilde{f}_{K^-p} - \tilde{f}_{K^-n}) \frac{1}{2}\rho_p}{1 + \frac{1}{4}\xi_k(\rho)\tilde{f}_0\rho(r)} + \frac{\tilde{f}_{K^-n}(\frac{1}{2}\rho_p + \rho_n)}{1 + \frac{1}{4}\xi_k(\rho)\tilde{f}_1\rho(r)} \right], \quad (5)$$

where  $\mu_K$  is the  $K^-$ -nucleus reduced mass and the in-medium  $K^-N$  scattering amplitudes in the  $K^-$ -nuclear c.m. frame,  $\tilde{f}_{K^-N}(\rho)$ , are related kinematically to the in-medium  $K^-N$  c.m. amplitudes  $f_{K^-N}(\rho)$  plotted in Figs. 1 and 2 by  $\tilde{f}_{K^-N}(\rho) = (1 + \frac{A-1}{A} \frac{\mu_K}{m_N}) f_{K^-N}(\rho)$ . These amplitudes, in view of Eq. (4), are now density dependent. The Pauli correlation factor  $\xi_k(\rho)$  is defined by [22]

$$\xi_k(\rho) = \frac{9\pi}{k_F^2} \left( 4 \int_0^\infty \frac{dr}{r} \exp(ikr) j_1^2(k_F r) \right), \quad (6)$$

with  $k = [(E_{K^-} - i\Gamma/2)^2 - m_K^2]^{1/2}$  and where  $\Gamma$  is the width of the particular kaonic atom state. The Fermi momentum is given by  $k_F = (3\pi^2\rho/2)^{1/3}$ ;  $\tilde{f}_0$  and  $\tilde{f}_1$  are the isospin 0 and 1 combinations, respectively, of the  $K^-N$  amplitudes; and  $\rho_p$  and  $\rho_n$  are proton and neutron densities, respectively. Denoting the integral in Eq. (6) by  $I_k(\rho)$ , it can be evaluated analytically,

$$4I_k(\rho) = 1 - \frac{q^2}{6} + \frac{q^2}{4} \left( 2 + \frac{q^2}{6} \right) \ln \left( 1 + \frac{4}{q^2} \right) - \frac{4}{3} q \left( \frac{\pi}{2} - \text{arctg}(q/2) \right), \quad (7)$$

with  $q = -ik/k_F$ . This expression corrects Eq. (A5) of Ref. [8]. The density dependence of  $\xi_k(\rho)\rho/4$  in the denominators of Eq. (5) reduces at threshold

to  $\xi_{k=0}(\rho)\rho/4 = (3k_F/2\pi) \propto \rho^{1/3}$ , thereby giving rise to a leading  $\rho^{4/3}$  Pauli-correlation contribution to the single-nucleon ‘ $t\rho$ ’ potential [22]

The single-nucleon optical potential  $V_{K^-}^{(1)}$  is often augmented by a phenomenological isoscalar potential  $V_{K^-}^{(2)}$  of the form

$$2\mu_K V_{K^-}^{(2)}(\rho) = -4\pi B \left(\frac{\rho}{\rho_0}\right)^\alpha \rho, \quad (8)$$

with a complex strength  $B$  and a positive exponent  $\alpha$ , representing  $K^-$  *multinucleon* processes. For  $\alpha = 1$ , the  $\rho^2$  dependence of  $V_{K^-}^{(2)}(\rho)$  agrees with that traditionally associated in mesic atoms with multinucleon meson interactions, motivated primarily by absorption on two nucleons [23, 24]. Although other effects as well could induce a  $\rho^2$  density dependence in leading order, e.g. self-energy (SE) insertions considered recently in Refs. [5, 6, 7], in this work we do not treat separately such  $\rho^2$  contributions. The added  $V_{K^-}^{(2)}(\rho)$  vanishes faster than  $\rho$  as  $\rho \rightarrow 0$ , and the in-medium  $K^-N$  amplitude given by the square bracket of Eq. (5) for  $V_{K^-}^{(1)}(\rho)$  agrees in this limit with that for free nucleons at threshold, consistently with the low density limit. Although  $V_{K^-}^{(2)}(\rho)$  is introduced independently of  $V_{K^-}^{(1)}(\rho)$ , it affects implicitly the density dependence of the in-medium  $V_{K^-}^{(1)}(\rho)$ , the latter being determined by a self consistent application of  $\delta\sqrt{s}(\rho)$ , Eq. (4), in which the *full* optical potential  $V_{K^-}(\rho) = V_{K^-}^{(1)}(\rho) + V_{K^-}^{(2)}(\rho)$  appears.

#### 2.4. Absorption at rest

Branching ratios of  $K^-$  absorption at rest on protons and on several nuclear species have been measured many decades ago with nuclear emulsions and with bubble chambers (BC). However, since the absorption fractions reported from the latter method are quoted with considerably smaller uncertainties than those of the former, we use here exclusively the results of three such BC experiments [11, 12, 13]. Davis et al. [11] quote  $0.26 \pm 0.03$  for the multinucleon capture fraction for  $K^-$  on a mixture of C, F and Br. Moulder et al. [12] quote  $0.28 \pm 0.03$  for that fraction on Ne, and the fraction for C is given by Vander Velde-Wilquet et al. [13] as  $0.19 \pm 0.03$ . We therefore adopt as a best estimate of an experimental  $K^-$  multinucleon absorption-at-rest fraction an average value of  $0.25 \pm 0.05$  for C and heavier nuclei. This may be linked with strong interaction level widths in kaonic atoms.

The level width  $\Gamma$  which is usually obtained from the complex eigenvalue  $E_{K^-} - i\Gamma/2$  when solving the Klein-Gordon equation with an optical potential



$V_{K^-}$  [10], is also related to the imaginary part of the potential by the overlap integral of  $\text{Im } V_{K^-}$  and  $|\psi|^2$ ,

$$\Gamma = -2 \frac{\int \text{Im } V_{K^-} |\psi|^2 d\vec{r}}{\int [1 - (B_{K^-} + V_C)/\mu_K] |\psi|^2 d\vec{r}}, \quad (9)$$

where  $B_{K^-}$ ,  $V_C$  and  $\mu_K$  are the  $K^-$  binding energy, Coulomb potential and reduced mass, respectively, and  $\psi$  is the  $K^-$  wave function of the particular state concerned [25]. For a Schrodinger equation the denominator is just the  $\psi$  normalization integral. When the optical potential  $V_{K^-}$  is the sum of a single-nucleon part  $V_{K^-}^{(1)}$  and a multinucleon part  $V_{K^-}^{(2)}$ , it is possible to apply Eq. (9) to each part, and thereby calculate single-nucleon and multinucleon absorption fractions, separately for any nucleus and for any specific kaonic atom state.

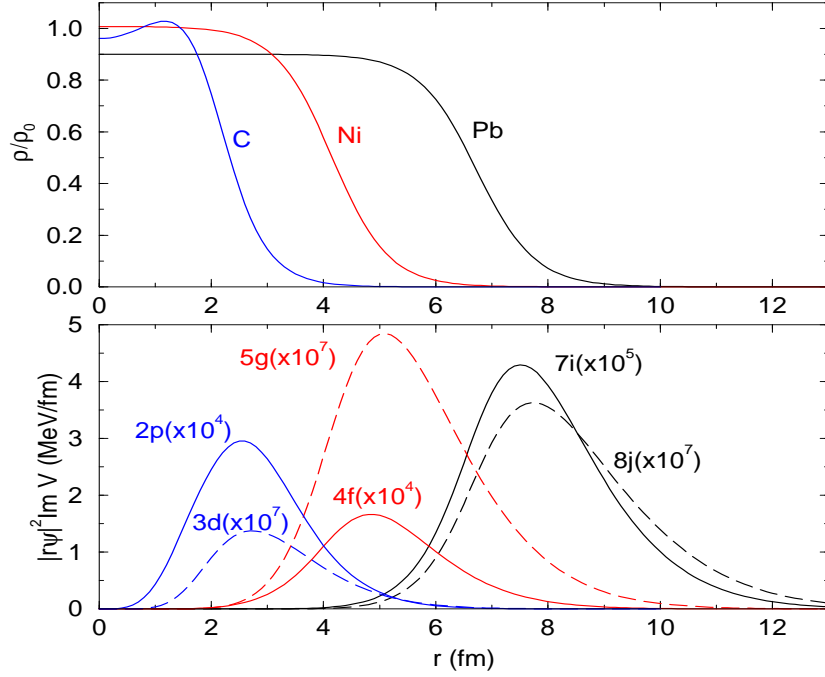


Figure 3: Color online. Lower panel:  $|r\psi|^2 \text{Im } V_{K^-}$  for several kaonic atoms for a ‘lower’ (solid curves) and an ‘upper’ (dashed curve) state. Top panel: the corresponding relative density distributions of the respective nuclei, with  $\rho_0=0.17 \text{ fm}^{-3}$ .

Figure 3 shows on the lower panel the overlap between kaonic atom wave functions and the imaginary potential for C, Ni and Pb, separately for the

‘lower’ and the ‘upper’ levels [25]. The wave functions were calculated from a best-fit phenomenological potential denoted DD in Ref. [10]. The upper panel of the figure shows the relative density distributions for these examples. The similarity between C, Ni and Pb is evident; the peak of the overlap for Ni and Pb is at densities near 15-20% of nuclear matter density for the lower state and at 10-15% for the upper state. These values are a little higher for C. In all cases the overlap extends inward to around 60% of central density, as found in [26]. As the width of a level is proportional to the integral of the overlap for a kaonic atom state with the imaginary potential Eq. (9), it is expected following Fig. 3 that absorption at rest of  $K^-$  mesons by nuclei will have very similar characteristic features for all targets from C and above along the periodic table. This is consistent with the limited data from BC experiments [11, 12, 13] that do not show any marked dependence of a multinucleon absorption fraction of  $0.25 \pm 0.05$  on the nuclear target. This value will serve here as a constraint on conventional analyses of strong-interaction observables in kaonic atoms.

### 3. Results

#### 3.1. Fits to kaonic atom data

As in earlier publications [9, 10] the present work deals with global analyses of kaonic atoms, handling together experimental results along the periodic table in order to gain insight on average properties of the  $K^-$ -nucleus interaction near threshold.

Table 1:  $\chi^2$  values for 65 kaonic atoms data points using exclusively single-nucleon optical potentials  $V_{K^-}^{(1)}(\rho)$ , Eq. (5), based on six chiral-model  $K^-N$  amplitudes. The density dependence of  $V_{K^-}^{(1)}(\rho)$  was determined by solving Eq. (4) self consistently.

model	B2	B4	M1	M2	P	KM
$\chi^2(65)$	1174	2358	2544	3548	2300	1806

Table 1 shows values of  $\chi^2$  for 65 kaonic atoms data points for an optical potential  $V_{K^-}^{(1)}(\rho)$  constructed from Eq. (5) using the six single-nucleon amplitudes from Cieplý et al. [3] shown in Figs. 1 and 2. As is clear from this table, none of these amplitudes leads to agreement with experiment. This

result is not new, as previous analyses have shown the need to include phenomenological terms motivated by  $K^-$  multinucleon processes,  $V_{K^-}^{(2)}$ , in order to obtain agreement with experiment [5, 6]. Equally good fits of  $\chi^2$  per point of less than 2 could also be achieved with purely phenomenological forms for  $V_{K^-}$  [9, 10].

Table 2: Best-fit parameters and  $\chi^2$  values for 65 kaonic atoms data points, from  $V_{K^-}^{(1)}$  optical potentials, Eq. (5), based on six chiral-model  $K^-N$  amplitudes, and supplemented by a  $V_{K^-}^{(2)}$  potential, Eq. (8), representing multinucleon  $K^-$  interactions. The density dependence of  $V_{K^-}^{(1)}(\rho)$  was determined by solving Eq. (4) with the full  $V_{K^-}$  self consistently. Correlations between  $\alpha$  and  $B$  cause some of the errors to be large.

model	B2	B4	M1	M2	P	KM
$\alpha$	0.29(10)	0.24(8)	0.24(16)	0.85(13)	1.4(1.2)	1.8(8)
Re $B$ (fm)	$2.3\pm 0.8$	$2.8\pm 0.3$	$0.2\pm 0.2$	$1.9\pm 0.4$	$-1.2\pm 0.3$	$0.1\pm 1.3$
Im $B$ (fm)	$0.8\pm 0.2$	$1.0\pm 0.1$	$0.7\pm 0.1$	$1.3\pm 0.2$	$2.4\pm 3.1$	$3.3\pm 1.1$
$\chi^2(65)$	111	105	121	108	125	122

At the next stage, we add to the single-nucleon part  $V_{K^-}^{(1)}$  a phenomenological part  $V_{K^-}^{(2)}$ , Eq. (8), in terms of an amplitude  $B(\rho/\rho_0)^\alpha$  with three parameters: a complex strength  $B$  and exponent  $\alpha > 0$ . Table 2 shows results of fits to the data obtained by varying these three parameters. The density dependence of the single-nucleon part  $V_{K^-}^{(1)}(\rho)$  of the full potential  $V_{K^-}$  was determined by solving self consistently Eq. (4) with the *full* potential  $V_{K^-}$ . It is seen that for each of the single-nucleon amplitudes that serve as the  $V_{K^-}^{(1)}$  basis for the overall potential  $V_{K^-}$ , a good fit is obtained. In some cases the uncertainties are large due mostly to correlations between  $B$  and  $\alpha$ . For the first three listed model amplitudes the values of  $\alpha$  are significantly smaller than 1, whereas for the other three  $\alpha$  is consistent with 1, meaning a  $\rho^2$  dependence of the potential.

A comment on uncertainties is in order. Although dealing with 65 kaonic atom data points, only 3–4 parameters can be obtained by fitting to these data, with very different sensitivities for the exponent  $\alpha$  and the other parameters. Once the single-nucleon part  $V_{K^-}^{(1)}$  serves as a fixed part of the optical potential  $V_{K^-}$ , the exponent is hard to fit, with consequences for the other parameters. In the present analysis, the uncertainties were derived from the covariant matrix, indicating correlations between parameters. Most of the

results in Table 2 demonstrate this problem which is overcome by scanning over  $\alpha$ .

Table 3: Same as in Table 2, except that  $\alpha$  is kept fixed at values compatible with its best-fit values.

model	B2	B4	M1	M2	P	KM
$\alpha$	0.3	0.3	0.3	1.0	1.0	1.0
Re $B$ (fm)	2.4±0.2	3.1±0.1	0.3±0.1	2.1±0.2	-1.3±0.2	-0.9±0.2
Im $B$ (fm)	0.8±0.1	0.8±0.1	0.8±0.1	1.2±0.2	1.5±0.2	1.4±0.2
$\chi^2(65)$	111	105	121	109	125	123

Table 3 shows results of fits when values of  $\alpha$  are kept fixed close to the best-fit values of Table 2. The  $\chi^2$  values are indeed as low as for the best fit when  $\alpha$  too was varied. The last two columns (P and KM) show essentially the same additional term ( $B$  and  $\alpha$ ) within uncertainties. Inspecting Fig. 1 and Fig. 2 it is seen that there are indeed great similarities between the two models, except at energies lower than 30 to 40 MeV below threshold. Although it could be argued that the values of  $\alpha$  for the first three listed amplitudes (B2, B4 and M1) are inconsistent with a plausible  $\rho^2$  dependence of the additional term, all six fits are essentially acceptable as fits to kaonic atom data. One needs additional constraints to narrow down the range of acceptable single-nucleon amplitudes.

Uncertainties in  $\alpha$  were taken into account by calculating best-fit values of  $B$  for  $\alpha$  between 1.0 and 2.5, thus making sure that these  $(B, \alpha)$  sets fit well the kaonic atom data. This provides the starting point for discussing the single-nucleon absorption fractions.

### 3.2. Fraction of single-nucleon absorptions

Fractions of absorption on a single nucleon were calculated for all 24 species of kaonic atoms included in the data base. These fractions were calculated from Eq. (9) separately for the lower and for the upper levels, using the six in-medium chiral-model  $K^-N$  amplitudes discussed above, supplemented by a phenomenological term  $B(\rho/\rho_0)^\alpha$  as given in Table 3.

Figure 4 shows calculated fractions of single-nucleon absorption when using the chiral-model input amplitudes P and KM. The two horizontal dashed lines represent our best estimate for the range of single-nucleon absorption

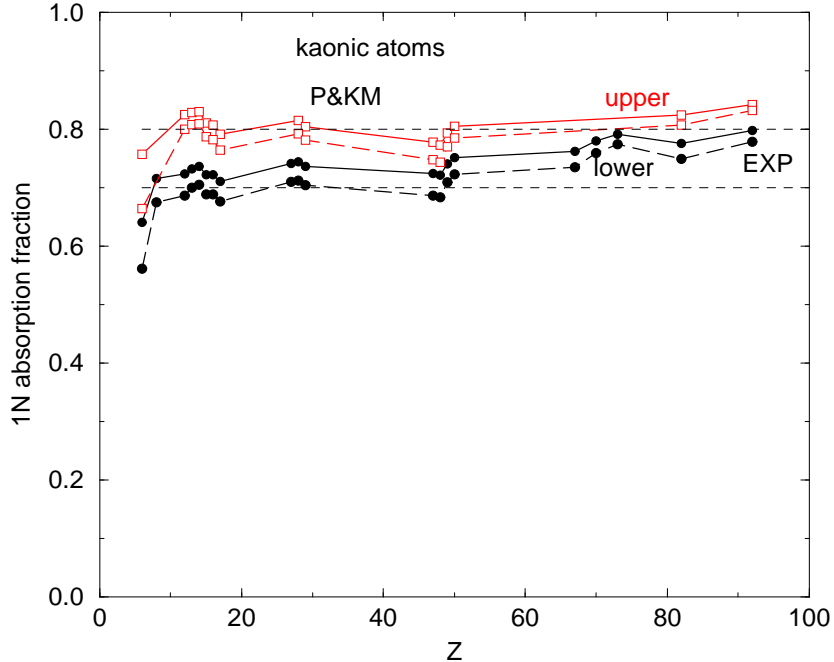


Figure 4: Color online. Fractions of single-nucleon absorption for amplitudes P and KM: solid circles are for lower states, open squares for upper states, solid curves use  $B$  values from Table 3 for  $\alpha=1$ , long-dashed curves use  $B$  values for  $\alpha=2$ . Horizontal dashed lines mark the range of experimental values of the single-nucleon absorption fraction. Models P and KM are indistinguishable from each other on this figure. See text for discussion of uncertainties.

fractions,  $0.75 \pm 0.05$ , as deduced from BC studies [11, 12, 13]. Solid circles represent lower states and open squares represent upper states. Solid curves are for  $\alpha=1$ , with best-fit values of the parameter  $B$  listed in Table 3. For  $\pm 10\%$  change of the input single-nucleon amplitudes, the calculated fractions change by  $\pm 0.4\%$ . To check sensitivity to fit parameters, the long-dashed curves are obtained from equally good fits to kaonic atoms data for  $\alpha=2$ , with  $B$  values given by

$$B_{\alpha=2}(\text{P}) = -0.5 + i4.6 \text{ fm}, \quad B_{\alpha=2}(\text{KM}) = 0.3 + i3.8 \text{ fm}. \quad (10)$$

Estimating the uncertainties arising from the phenomenological part  $V_{K^-}^{(2)}$  of the optical potential, the calculated fractions change by  $\pm 4\%$  upon using extreme values of  $\alpha$  between 1 and 2, and up to  $\pm 0.6\%$  upon using the

results of Table 3. These estimated uncertainties are comfortably below the experimental uncertainty given by the two horizontal dashed lines in Fig. 4.

The results for the P and KM sets of amplitudes are indistinguishable on the scale of the figure. Indeed, Figs. 1 and 2 show that the two sets of amplitudes are very similar to each other over most of the energy range between threshold and 30-40 MeV below. This is the subthreshold energy range reached by applying the density-to-energy transformation Eq. (4) for densities as high as 50% of  $\rho_0$ . The contribution to the level widths from higher density regions is suppressed owing to the poor overlap of the atomic wave functions with the nucleus at these densities.

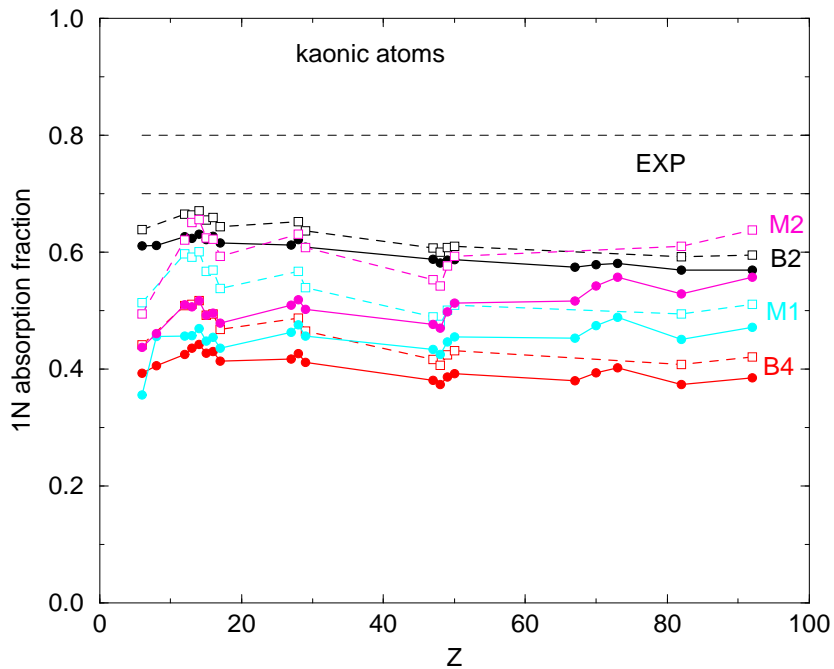


Figure 5: Color online. Fractions of single-nucleon absorption for amplitudes B2, B4, M1 and M2, using  $\alpha$  and  $B$  values from Table 3. Solid circles and solid curves are for lower states, open squares and long-dashed curves are for upper states. Horizontal dashed lines mark the range of experimental values. See text for discussion of uncertainties.

In comparing between calculation and experiment we note that for almost all species of kaonic atoms in the data base, the absorptions from the upper state are of the order of 10-15% of all absorptions, as deduced from the mea-

sured upper level to lower level radiation yields. Carbon is an exception with, by far, the lowest *radiation* yield (of  $0.07 \pm 0.013$ ). Atomic cascade calculations show that for C about 75% of the absorptions take place from the upper state. Therefore the calculated single-nucleon absorption fractions should be close to the upper level points for C and very close to the lower level points for all the other species. We conclude that the agreement of calculations based on the P and KM amplitudes with the estimated experimental range for the single-nucleon absorption fractions is very good.

Figure 5 shows comparisons between calculations and the experimental range for the other four potentials, using  $\alpha$  and  $B$  values listed in Table 3. Again, solid circles are for lower states and open squares are for upper states. The computed values of single-nucleon absorption fractions for these potentials, as shown in the figure, fall short significantly of the range of values deduced from bubble-chamber experiments. Thus, it is evident that none of these potential models is in agreement with experiment.

#### 4. Discussion

With the construction of in-medium  $K^-N$  amplitudes as detailed above, it is desirable to re-examine several issues discussed in earlier studies of purely phenomenological  $K^-$  nuclear optical potentials. In these studies, the simplest possible phenomenological ‘ $t\rho$ ’ optical potential of the form

$$2\mu_{K^-} V_{K^-}^{t\rho} = -4\pi b \rho \quad (11)$$

was adopted, with a density independent isoscalar complex amplitude  $b$ , leading to reasonably good fits to kaonic atom data [9, 10]. However, the fitted constant amplitude  $b$  did not reflect any known property of the  $K^-$  nuclear interaction, and the real and imaginary parts of  $V_{K^-}^{t\rho}$  in the nuclear interior were merely extrapolations from the surface region. Imposing the low-density limit by requiring a slightly repulsive threshold amplitude  $b^{(\text{th})}$  and adding a phenomenological isoscalar density-dependent term,

$$b \rightarrow b^{(\text{th})} + B \left( \frac{\rho}{\rho_0} \right)^\alpha, \quad \alpha > 0, \quad (12)$$

improved fits were obtained, associated with compression of the real part of the potential [27]. However, the dependence on density, in particular the density independence of the single-nucleon term  $b^{(\text{th})}$ , did not result from

any microscopic model. Thus, extrapolations to the nuclear interior were biased by the simple ansatz (12). In contrast, the present formulation of a single-nucleon part  $V_{K^-}^{(1)}$  of the  $K^-$ -nucleus optical potential is based on a *microscopic* model approach to the free-space energy dependent  $K^-N$  amplitude and to the way it evolves into a single-nucleon in-medium amplitude. Phenomenology enters in our construction only by adding a multinucleon part  $V_{K^-}^{(2)}$ . This approach was developed in a series of recent works [5, 6, 7, 8].

Having chosen within the present approach a preferred set of  $K^-N$  amplitudes (sets P and KM are essentially equivalent in this respect), it is instructive to examine in detail the KM *in-medium* single-nucleon and full amplitudes. This is done in the next two subsections, while in the third subsection we remark on the role of ‘subthreshold kinematics’ in absorption-at-rest calculations.

#### 4.1. Interplay between theory and phenomenology

Here we discuss the geometry of best-fit  $K^-$  nuclear amplitudes and optical potentials. Recalling Eq. (5) for  $V_{K^-}^{(1)}$ , we define the expression within the square brackets on the r.h.s. as the in-medium  $K^-N$  amplitude times  $\rho$ . Likewise for  $V_{K^-} = V_{K^-}^{(1)} + V_{K^-}^{(2)}$ , the expression  $-(2\mu_{K^-}/4\pi)V_{K^-}(\rho)$  may be defined as the full in-medium amplitude times  $\rho$ . Figure 6 shows, as an example, in-medium scattering amplitudes as function of the relative density in the Ni nucleus. Plotted in the upper panel are in-medium single-nucleon  $K^-N$  amplitudes, averaged over protons and neutrons, from the KM chiral model, for two choices of the multinucleon phenomenological exponent  $\alpha$ . The slight dependence on  $\alpha$  observed in this panel is due to the dependence of  $\delta\sqrt{s}$  on the full optical potential in Eq. (4). Plotted in the lower panel are full in-medium amplitudes, including the added phenomenological term  $B(\rho/\rho_0)^\alpha$ . It is seen that up to a density of 40–50% of central density  $\rho_0$  the two values of  $\alpha$  lead to about the same imaginary parts of the amplitudes (and potentials). Recall that both values of  $\alpha$ , and the associated complex values of the parameter  $B$ , were obtained from best fits to the kaonic atoms data. The model dependence of the real part of the full in-medium amplitude is stronger, reflecting the fact that for kaonic atoms the imaginary part of the potential is dominant. In fact, strong interaction level widths are significantly larger than the corresponding level shifts in kaonic atoms. Clearly, the full in-medium amplitudes (and potentials) for densities greater than 40–50% of central density are just analytical continuation of whatever parameterization was employed for the phenomenological terms.



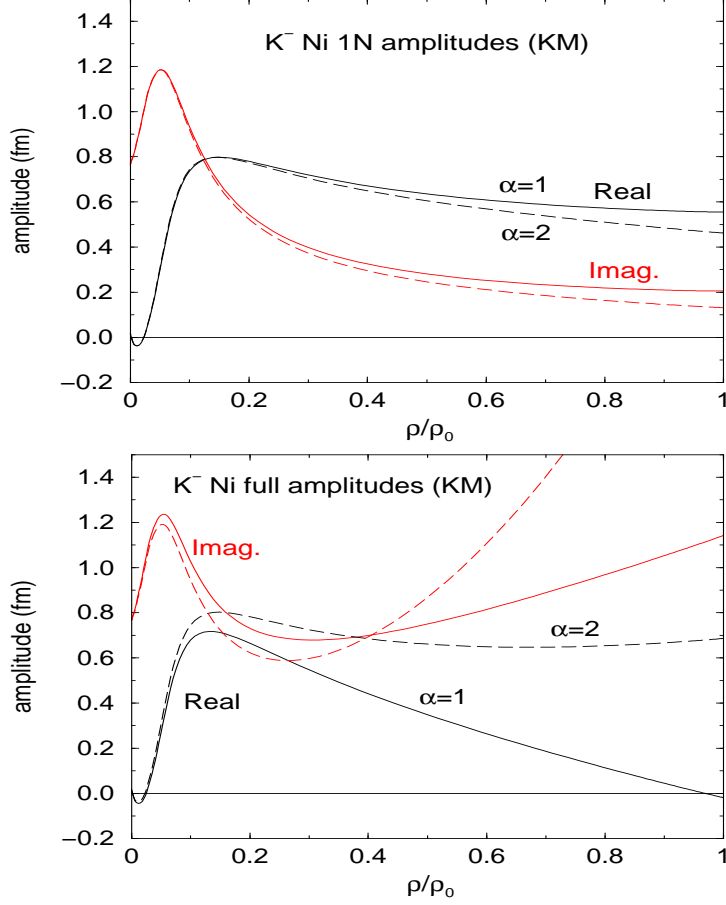


Figure 6: Color online. Upper panel: in-medium single-nucleon  $K^-N$  amplitudes in Ni from best fits to 65 kaonic-atoms data points, using the free-space KM model amplitudes in  $V_{K^-}^{(1)}$ , Eq. (5), plus a phenomenological multinucleon amplitude  $B(\rho/\rho_0)^\alpha$  in  $V_{K^-}^{(2)}$ , Eq. (8), with  $\alpha=1$  (solid curves) and  $\alpha=2$  (dashed curves). Eq. (4) with the full  $V_{K^-}$  was solved self consistently to obtain the density dependence of  $V_{K^-}^{(1)}$ . Lower panel: the *full* in-medium  $K^-$  amplitudes corresponding to  $V_{K^-} = V_{K^-}^{(1)} + V_{K^-}^{(2)}$ . See text for definitions.

Systematics of purely phenomenological  $K^-$ -nucleus optical potentials showed [27] that the r.m.s. radius of the real part was usually smaller than the corresponding radius of the density distribution of the nucleus. This can be attributed to the sharp rise of the real part of the full in-medium amplitude with increased density near the nuclear surface. Figure 6 shows that a similar

rise of the imaginary part of the full in-medium amplitude is followed, still in the surface region, by a decrease as the density increases, which could cause the reverse trend in the r.m.s. radius. Indeed, phenomenological potentials show that the r.m.s. radius of the imaginary part can be either somewhat larger or smaller than that of the nucleus.

#### 4.2. Radial sensitivity of kaonic atoms

The issue of radial sensitivity of kaonic atom experiments is examined next. Figure 7 shows, as an example, three versions of optical potentials for Ni that fit equally well the whole set of kaonic atoms data across the periodic table. The KM potentials for  $\alpha=1$  and  $\alpha=2$  consist of a single-nucleon potential  $V_{K^-}^{(1)}$  (5) based on the KM  $K^-N$  amplitudes, augmented by a phenomenological potential  $V_{K^-}^{(2)}$  (8) with a complex parameter  $B$  listed in Table 3 for  $\alpha=1$  and in Eq. (10) for  $\alpha=2$ . Both of these KM versions of  $V_{K^-}$  satisfy the low-density limit and reproduce well the experimentally based single-nucleon absorption-at-rest fractions considered in the present work. In contrast, the third potential, a purely phenomenological density-dependent potential of the form (12) with  $\alpha=1$ , does not necessarily respect any of these constraints. The potentials are plotted as function of the density, relative to nuclear matter density  $\rho_0$ . It is seen that for the imaginary part of the potential all three curves almost coincide up to 40% of  $\rho_0$ , and only above 50% of  $\rho_0$  they begin to depart from each other. The real parts differ from each other already above 30% of  $\rho_0$ . The wild disagreement between these models for densities larger than 60% of  $\rho_0$ , in spite of all three potentials producing equally good fits to the data, indicates that kaonic atoms are totally insensitive to these density regions in nuclei. This is in line with the overlaps presented in Fig. 3 for the atomic wave functions and the imaginary part of the potential. The strength of the well-defined imaginary part of the potential in the nuclear surface region ensures damping of the atomic wave function when the density exceeds about 50% of  $\rho_0$ . The potential in the surface region is dominated by the single-nucleon amplitudes that are firmly rooted in theory and are validated here, upon introducing a best-fit phenomenological potential  $V_{K^-}^{(2)}$ , by the single-nucleon absorption fraction constraint.

As noted above, the behavior of  $\text{Re } V_{K^-}(\rho)$  at densities beyond  $\approx 0.2 \rho_0$ , as shown in the upper panel of Fig. 7, represents merely extrapolation to a density regime which is uncontrolled by fitting to kaonic atoms data. Yet, one cannot avoid the question of why the resulting depth of  $\text{Re } V_{K^-}(\rho)$  at

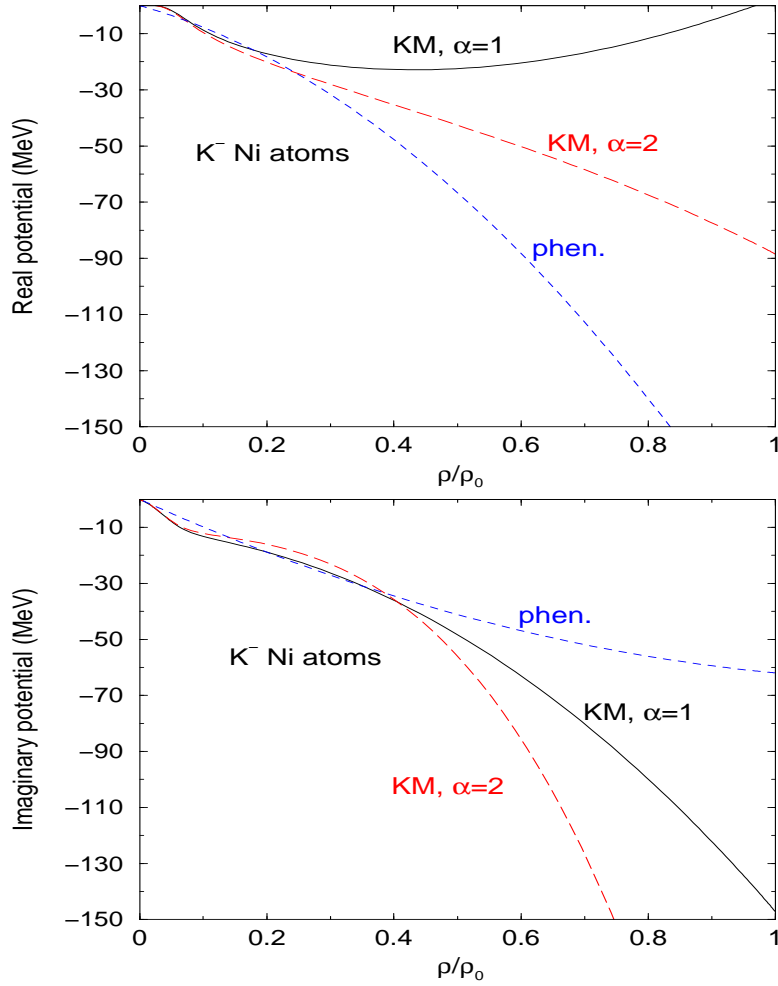


Figure 7: Color online. Real part (upper panel) and imaginary part (lower panel) of best-fit  $K^-$  optical potentials for kaonic atoms of Ni. Solid curves and long-dashed curves are based on the KM single-nucleon amplitudes plus a phenomenological term  $B(\rho/\rho_0)^\alpha$ , dashed curves are for a purely phenomenological density-dependent best-fit potential [10]. All three potentials lead to equally good fits to the 65 data points in kaonic atoms.

nuclear matter density  $\rho_0$  in the two KM versions shown is so much smaller than that produced in the purely phenomenological model [10], also shown in the figure, and in more recent analyses based on single-nucleon  $\bar{K}N$  chiral approaches [7, 8]. To answer this query we note that the added  $V_{K^-}^{(2)}$  in the latter works consisted of two terms, one linear and the other approximately

quadratic in the nuclear density. The linear term was interpreted as possibly correcting the the single-nucleon input of  $V_{K^-}^{(1)}$ , and it came out *repulsive* by fitting to the data whereas the quadratic term came out *attractive*. At  $\rho \lesssim 0.2\rho_0$ , where the fit is still meaningful, the overall sign of  $V_{K^-}^{(2)}$  was determined by the repulsive linear term, but at larger densities the quadratic term took over and made  $V_{K^-}^{(2)}$  attractive. In the present work we insist on respecting the low density limit which rules out including a linear (in the density) term beyond  $V_{K^-}^{(1)}$ . The role of this linear term in the previous analyses [7, 8] is now taken over by the only multinucleon term represented by the complex  $B$  parameter, so it now comes *repulsive* in most fits. This example demonstrates explicitly how the high density behavior of  $\text{Re } V_{K^-}(\rho)$  is no more than just extrapolation based on whatever parametrization, valid at the low-density regime, one uses in the analysis.

#### 4.3. Role of ‘subthreshold kinematics’ in absorption-at-rest calculations

The present calculations of single-nucleon absorption fractions make use of the ‘subthreshold kinematics’ formulation to evaluate self consistently the in-medium single-nucleon part  $V_{K^-}^{(1)}(\rho)$  of the  $K^-$  nuclear optical potential  $V_{K^-}$  applicable in kaonic atoms. In this formulation, the downward energy shift  $\delta\sqrt{s}$  at which the free-space  $K^-N$  scattering amplitudes need to be evaluated in the nuclear medium, translates into a density dependence of the in-medium scattering amplitudes. A major contribution to this  $\delta\sqrt{s}$ , Eq. (4), arises from the nonvanishing in-medium kaon momentum  $p_{K^-}$ , related in the local density approximation to  $V_{K^-}$  as given by Eq. (2). We recall that a  $K^-$  meson orbiting in kaonic atoms is not at rest when exposed to the strong-interaction nuclear force. Here we wish to demonstrate the significant effect of this kaon-momentum contribution on the  $K^-$  absorption fractions calculated in Sect. 3.2 and compare with other calculations that disregard it.

Table 4 lists single-nucleon absorption fractions for the lower and upper states in kaonic Ni atoms, as calculated in the present work and shown in Figs. 4 and 5, using the three model amplitudes that allow in their best fits a multinucleon term  $V_{K^-}^{(2)}(\rho)$  with  $\alpha=1$ . Since most of the absorption in kaonic Ni occurs from the lower state, the table demonstrates that models KM and P reproduce the experimentally deduced single-nucleon absorption fraction of  $0.75\pm 0.05$ , whereas model M2 fails to do so by a wide margin.

Table 5 is constructed similarly to Table 4, but the contribution of the kaon momentum  $p_{K^-}$  to the r.h.s. of Eq. (4) is switched off. The  $\chi^2$  values

Table 4: Best-fit values of  $\text{Re} B$  and  $\text{Im} B$  for  $\alpha=1$ , and single-nucleon fractions of absorption from the lower and upper states in the kaonic Ni atom, for three model amplitudes used to evaluate  $V_{K^-}(\rho)$ .

amplitude	$\chi^2(65)$	$\text{Re}B$ (fm)	$\text{Im}B$ (fm)	lower	upper
KM	122	$-0.9\pm 0.2$	$1.4\pm 0.2$	0.74	0.81
P	125	$-1.3\pm 0.2$	$1.5\pm 0.2$	0.73	0.80
M2	109	$2.1\pm 0.2$	$1.2\pm 0.2$	0.52	0.63

Table 5: Same as in Table 4, except that  $\delta\sqrt{s}$  of Eq. (4) is modified by assuming that the in-medium  $K^-$  momentum  $p_{K^-}$  is zero, see text.

amplitude	$\chi^2(65)$	$\text{Re}B$ (fm)	$\text{Im}B$ (fm)	lower	upper
KM	140	$-1.3\pm 0.2$	$0.8\pm 0.2$	0.85	0.89
P	141	$-1.6\pm 0.2$	$0.9\pm 0.2$	0.84	0.89
M2	159	$0.0\pm 0.1$	$1.3\pm 0.2$	0.67	0.76

of these best-fits are not as good as those listed in Table 4 and the single-nucleon fractions calculated in models KM and P no longer reproduce the experimental ones. The general trend of the calculated single-nucleon absorption fractions is to increase with this modification of  $\delta\sqrt{s}$  in Eq. (4). This still leaves model M2 unacceptable as far as absorption from the dominant lower state is concerned, although it brings the fraction calculated for absorption from the upper state into accordance with experiment. Note that the values of  $\delta\sqrt{s}$  for  $p_{K^-} = 0$  are smaller by about 10 MeV with respect to those obtained with full account of  $p_{K^-}$  according to Eq. (2). The variation of  $\text{Im} V_{K^-}$  over this energy interval is sufficiently strong to cause this increase in the calculated single-nucleon absorption fractions.

Finally, we comment on the nuclear-matter calculation of  $K^-$  absorption fractions in Ref. [15], in particular those shown in Fig. 17. In this work a microscopic model, using meson-exchange contributions dominated by the subthreshold  $\Lambda^*(1405)$  resonance, was formulated for the absorptive parts of *both*  $V_{K^-}^{(1)}(\rho)$  and  $V_{K^-}^{(2)}(\rho)$ . The single-nucleon absorption fraction decreases in this calculation from the value 1 for  $\rho \rightarrow 0$ , reaching the experimentally deduced value of  $0.75\pm 0.05$  at a density about 70–90% of  $\rho_0$ , which is too

high value compared to where absorption takes place in kaonic atoms. At typical kaonic atoms absorption densities of 30–40% of  $\rho_0$ , the single-nucleon absorption fraction calculated in this model is about 0.85 to 0.90. This should decrease, according to the insight gained by comparing the absorption fractions listed in Table 5 with those in Table 4, once the assumption of  $K^-$  at rest is relaxed in the calculations of Ref. [15], perhaps offering a better agreement with experiment.

## 5. Summary

Six recent sets of  $K^-N$  amplitudes near threshold, based on SU(3) chiral-model EFT approaches to the  $\bar{K}$ -nucleon interaction, have been tested as basic components in the construction of  $K^-$ -nucleus optical potentials that fit kaonic atom strong-interaction data across the periodic table. All sets need to be supplemented by a phenomenological term in order to fit the data. However, imposing as additional constraint the single-nucleon fraction of absorption at rest, only two of the six  $K^-N$  model amplitudes are found capable of reproducing the absorption fractions obtained from bubble-chamber experiments. The two acceptable models, marked as KM for Kyoto-Munich and P for Prague, produce very similar in-medium  $\bar{K}N$  amplitudes down to about 40 MeV below threshold, which is the region of energies relevant for kaonic atoms.

## Acknowledgements

We thank Aleš Cieplý for providing us with  $K^-N$  amplitudes from Ref. [3] in tabulated form. Useful remarks by him and by Jiří Mareš on the penultimate version of this work are gratefully acknowledged.

## References

- [1] M. Bazzi, et al. (SIDDHARTA Collaboration), Phys. Lett. B 704 (2011) 113.
- [2] M. Bazzi, et al. (SIDDHARTA Collaboration), Nucl. Phys. A 881 (2012) 88.
- [3] A. Cieplý, M. Mai, U.-G. Meißner, J. Smejkal, Nucl. Phys. A 954 (2016) 17.

- [4] Y. Kamiya, K. Miyahara, S. Ohnishi, Y. Ikeda, T. Hyodo, E. Oset, W. Weise, Nucl. Phys. A 954 (2016) 41.
- [5] A. Cieplý, E. Friedman, A. Gal, D. Gazda, J. Mareš, Phys. Lett. B 702 (2011) 402.
- [6] A. Cieplý, E. Friedman, A. Gal, D. Gazda, J. Mareš, Phys. Rev. C 84 (2011) 045206.
- [7] E. Friedman, A. Gal, Nucl. Phys. A 881 (2012) 150.
- [8] E. Friedman, A. Gal, Nucl. Phys. A 899 (2013) 60.
- [9] C.J. Batty, E. Friedman, A. Gal, Phys. Rep. 287 (1997) 385.
- [10] E. Friedman, A. Gal, Phys. Rep. 452 (2007) 89.
- [11] H. Davis, F. Oppenheimer, W.L. Knight, F.R. Stannard, O. Treutler, Nuovo Cimento 53A (1968) 313.
- [12] J.W. Moulder, N.E. Garrett, L.M. Tucker, W.M. Bugg, G.T. Condo, H.O. Cohn, R.D. McCulloch, Nucl. Phys. B 35 (1971) 332.
- [13] C. Vander Velde-Wilquet, J. Sacton, J.H. Wickens, D.N. Tovee, D.H. Davis, Nuovo Cimento 39A (1977) 538.
- [14] J. Yamagata, S. Hirenzaki, Eur. Phys. J. A 31 (2007) 255.
- [15] T. Sekihara, J. Yamagata-Sekihara, D. Jido, Y. Kanada-En'yo, Phys. Rev. C 86 (2012) 065205.
- [16] Y. Ikeda, T. Hyodo, W. Weise, Phys. Lett. B 706 (2011) 63, Nucl. Phys. A 881 (2012) 98.
- [17] A. Cieplý, J. Smejkal, Nucl. Phys. A 881 (2012) 115.
- [18] Z.H. Guo, J.A. Oller, Phys. Rev. C 87 (2013) 035202.
- [19] M. Mai, U.-G. Meißner, Eur. Phys. J. A 51 (2015) 30.
- [20] T.E.O. Ericson, L. Tauscher, Phys. Lett. B 112 (1982) 425.
- [21] E.E. Kolomeitsev, N. Kaiser, W. Weise, Phys. Rev. Lett. 90 (2003) 092501.

- [22] T. Waas, M. Rho, W. Weise, Nucl. Phys. A 617 (1997) 449.
- [23] M. Ericson, T.E.O. Ericson, Ann. Phys. 36 (1966) 323.
- [24] R. Seki, K. Masutani, Phys. Rev. C 27 (1983) 2799.
- [25] E. Friedman, S. Okada, Nucl. Phys. A 915 (2013) 170.
- [26] N. Barnea, E. Friedman, Phys. Rev. C 75 (2007) 022202(R).
- [27] E. Friedman, A. Gal, C.J. Batty, Phys. Lett. B 308 (1993) 6.